

# DuoMo: Dual Motion Diffusion for World-Space Human Reconstruction

Yufu Wang<sup>1,2</sup> Evonne Ng<sup>1</sup> Soyong Shin<sup>1,3</sup> Rawal Khirodkar<sup>1</sup> Yuan Dong<sup>1</sup> Zhaoen Su<sup>1</sup>  
 Jinhyung Park<sup>1,3</sup> Kris Kitani<sup>1,3</sup> Alexander Richard<sup>1</sup> Fabian Prada<sup>1</sup> Michael Zollhöfer<sup>1</sup>  
<sup>1</sup> Meta Reality Labs <sup>2</sup> University of Pennsylvania <sup>3</sup> Carnegie Mellon University

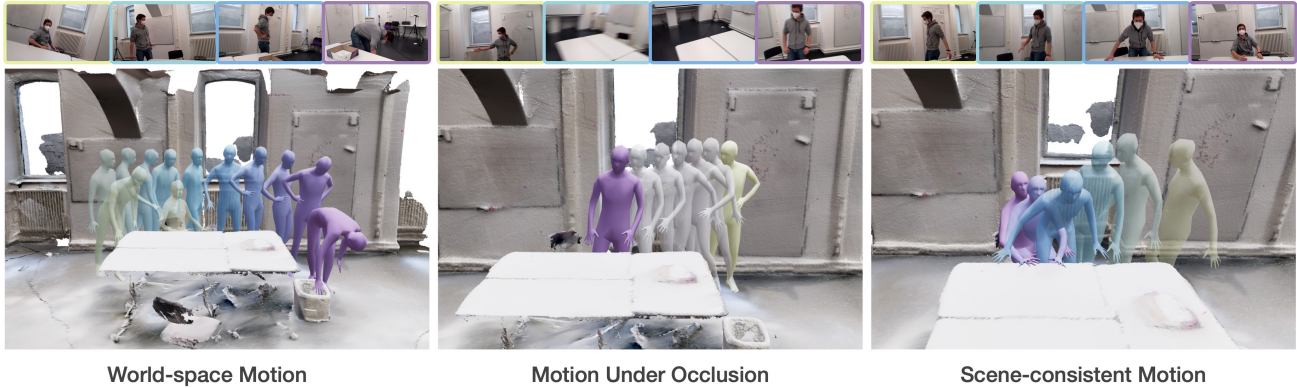


Figure 1. **Dual Motion Diffusion (DuoMo)** recovers world-space human motion from unconstrained monocular videos. Our two-prior approach reconstructs accurate world-space motion (left), completes motion under occlusion or missing observation (middle), and generates scene-consistent motion with guided sampling (right). Moreover, our method outputs the mesh vertices directly without a SMPL model.

## Abstract

We present *DuoMo*, a generative method that recovers human motion in world-space coordinates from unconstrained videos with noisy or incomplete observations. Reconstructing such motion requires solving a fundamental trade-off: **generalizing** from diverse and noisy video inputs while maintaining **global motion consistency**. Our approach addresses this problem by factorizing motion learning into two diffusion models. The camera-space model first estimates motion from videos in camera coordinates. The world-space model then lifts this initial estimate into world coordinates and refines it to be globally consistent. Together, the two models can reconstruct motion across diverse scenes and trajectories, even from highly noisy or incomplete observations. Moreover, our formulation is general, generating the motion of mesh vertices directly and bypassing parametric models. *DuoMo* achieves state-of-the-art performance. On EMDB, our method obtains a 16% reduction in world-space reconstruction error while maintaining low foot skating. On RICH, it obtains a 30% reduction in world-space error. Project page: [yufu-wang.github.io/duomo/](https://yufu-wang.github.io/duomo/)

## 1. Introduction

Perceiving human motion within the 3D world is a fundamental aspect of understanding human behavior [6, 51]. When viewing a video, humans effortlessly build a coherent mental model of the scene [56]: we distinguish the subject’s movement from the camera’s motion, track their trajectories through the environment, and infer their interaction with the world. This perception involves seamlessly integrating a local, view-dependent understanding of a person’s pose with a global, persistent model of the world and the motion in it. Replicating this capability in computer vision, however, remains a significant challenge, especially when dealing with unconstrained videos captured by moving cameras.

The focus of human motion modeling in computer vision has recently shifted from analyzing isolated pose sequences to recovering motion grounded in a consistent world coordinate system. This advancement is supported by progress in camera motion estimation and world-space motion capture data. However, current methods face a fundamental trade-off between generalizability and global consistency. On one hand, end-to-end models [38, 61, 62] can learn powerful priors to predict human motion in world coordinates. However, they often fail to generalize in complex scenes, as they are limited by the motion diversity of the studio-captured

data. On the other hand, approaches that first model pose in the camera coordinates and then “lift” the motion into the world using camera parameters are more robust to diverse motion in the wild [76, 77]. However, their motion priors are inherently local and often too weak to enforce physical plausibility and consistency in world coordinates.

To address this trade-off, we introduce Dual Motion Diffusion (DuoMo), a method that factors the problem into a two-stage generative process. Instead of committing to a single representation, our approach leverages the strengths of both camera-space and world-space motion modeling by training two independent generative models:

- *a model for camera-space motion* learns a generalizable prior that reconstructs human motion from the camera’s perspective, and
- *a model for world-space motion* learns a prior of plausible and consistent human motion in a global coordinate system.

Our key insight lies in how we connect these two models. Instead of forcing a single, end-to-end model to learn this complex geometric relationship, we inject this known geometric principle directly into the pipeline. Specifically, the camera-space model’s output is explicitly lifted into the world coordinates using the estimated camera motion.

This design choice allows us to effectively structure our system as a two-stage generative process. The camera-space model acts as the initial estimation stage, focusing on interpreting video frames and reconstructing motion with respect to the viewpoint. The explicit lifting step transforms its output into world coordinates, which become a noisy proposal for the world-space motion. All sources of error — from camera pose estimates, depth ambiguity, and the first model’s own imperfections — are exposed as noise in the proposal. The world-space model then functions as a global refinement stage, whose task is to take this noisy, incomplete proposal and refine it to be physically plausible and globally consistent.

Our second insight lies in how we define the coordinate system for our world-space model. Many existing methods [57, 71, 90] are trained to operate directly in the canonical coordinate system provided by studio capture datasets (e.g., a lab space where the Y-axis is ‘up’ and the ground is flat at zero height). To use such a model, a reconstruction system must align its camera-space human motion with this canonical space. This alignment requires estimating the camera’s pose relative to the scene’s ground plane—a step that is ambiguous, error-prone, and often impossible for in-the-wild videos on varied terrain like hills or stairs.

We sidestep this alignment problem entirely. DuoMo’s world-space model is not tied to a fixed, canonical coordinate system. Instead, we define the world coordinates for each video relative to its starting camera pose. Our world-space model is then trained to denoise motion di-

rectly within these diverse, per-video coordinate systems, without any canonical transformation. This approach is not just simpler; it allows our model to reconstruct plausible motion in complex, in-the-wild scenes.

Finally, our approach is general with respect to the motion representation. Rather than learning to generate the low-dimensional parameters of a body model like SMPL [47], our diffusion models generate the motion of the mesh vertices themselves. This shows that our architecture can model geometric motion directly, suggesting a more general path for modeling motion in other categories [60].

We conduct experiments on EMDB [29], RICH [24] and Egobody [89], and demonstrate substantial improvement in world-space motion accuracy and robustness. To summarize, our main contributions are:

- DuoMo, a two-stage diffusion method that decouples human motion reconstruction into a camera-space estimation stage and a world-space refinement stage;
- a world-space motion model trained to denoise motion in per-video coordinate systems, making it robust to in-the-wild scenes; and
- an architecture that generates the motion of mesh vertices directly, without relying on parametric body models.

## 2. Related work

**Human motion reconstruction.** Reconstructing 3D human pose and shape from monocular images [7, 27, 32, 33, 36, 40, 67, 86] and videos [2, 10, 26, 31, 78] has been extensively studied in computer vision. Recent advances in transformer architectures [13, 74], large-scale datasets [5, 49], and parametric body models [46, 54, 79] have enabled state-of-the-art methods [4, 19, 53, 60, 77] to achieve high accuracy on challenging benchmarks [25, 75].

While these methods excel at local pose and shape estimation, reconstructing motion in a consistent world coordinate system remains a significant challenge and has become a recent focus [20, 28, 37, 44, 83]. Current methods for this task broadly fall into two categories: lifting-based and direct prediction. The “lifting” approach first reconstructs humans in the camera’s coordinate system [9, 76, 77, 82] and then transform them to world coordinates using estimated cameras [69, 70], often followed by post-hoc refinement steps [1, 45, 82]. In contrast, the “direct prediction” approach trains a network to regress the human motion in a global coordinate [38, 61, 62, 68]. Our method begins with the “lifting” approach, employing a camera-space motion diffusion model as an initial step. Unlike previous methods that rely on post-hoc optimization, we introduce a world-space motion diffusion model to refine the final predictions in world space.

**Generative models for motion reconstruction.** Generative models [23, 30, 73] have shown great success in differ-

ent human motion generation tasks [8, 21, 39, 43, 71, 87]. Applying them for reconstruction tasks presents unique challenges. One line of work employs pre-trained motion priors within an optimization-based framework [48, 57, 65, 72]. However, a significant drawback is the computational cost [22, 57, 82]. For faster inference, other work trains conditional generative models to estimate pose or motion [14, 35, 59] based on visual inputs, demonstrating potential to resolve visual ambiguities [18]. Recent works extend this direction to generate human motion in a consistent global coordinate system [38, 90]. Our work reconstructs global human motion with generative models but factors into two priors to gain robustness and generalization.

### 3. Method

We consider the problem of reconstructing world-space human motion from unconstrained video. An overview is given in Fig 2. The camera-space model encodes video features and generates human motion in camera coordinates. This motion is transformed to the world coordinates using camera poses, and becomes an initial noisy proposal for world-space motion. The world-space model encodes this noisy proposal and generates clean and coherent world-space human motion.

#### 3.1. Motion representation

We represent the human body as vertices on a 3D mesh  $\mathbf{X} \in \mathbb{R}^{V \times 3}$ . We denote the human body state at video time  $t$  in coordinate system  $a$  as  ${}^a\mathbf{X}_t$ . With this convention, the camera-space motion ( $\mathbf{C}$ ) is the motion sequence where each frame’s state is in its own instantaneous camera coordinates. The full camera-space motion sequence is

$$\mathbf{C} = ({}^1\mathbf{X}_1, {}^2\mathbf{X}_2, \dots, {}^T\mathbf{X}_T). \quad (1)$$

For each video, we define a unique world coordinate system by setting the initial camera pose as the origin, and subsequently measuring all motion relative to it. The world-space human motion ( $\mathbf{W}$ ) is a fixed coordinate system with respect to the camera of the first video frame,

$$\mathbf{W} = ({}^1\mathbf{X}_1, {}^1\mathbf{X}_2, \dots, {}^1\mathbf{X}_T). \quad (2)$$

The camera-space and world-space motion are related by camera poses at each timestep. Let  $\mathbf{g}_t$  be the camera pose that maps the  $t$ -th camera coordinates to the world coordinates (camera 1). We can ‘lift’ the camera-space motion  $\mathbf{C}$  to world-space motion  $\mathbf{W}$  using the camera motion

$${}^1\hat{\mathbf{X}}_t = \mathbf{g}_t({}^t\mathbf{X}_t). \quad (3)$$

where the hat operator denotes ‘lifted’ variables.

Our goal is to train diffusion models to generate  $\mathbf{C}$  and  $\mathbf{W}$ . To ensure numerical stability, we decompose  $\mathbf{X}$  as follows: in camera space, each state  ${}^t\mathbf{X}_t$  is decomposed as

the root-centered mesh  ${}^t\mathbf{P}_t \in \mathbb{R}^{V \times 3}$  and the root position  ${}^t\mathbf{r}_t \in \mathbb{R}^3$  so that  ${}^t\mathbf{X}_t = {}^t\mathbf{P}_t + {}^t\mathbf{r}_t$ . Our camera-space model generates  $({}^t\mathbf{P}_t, {}^t\mathbf{r}_t)$ . In the world space,  ${}^1\mathbf{r}_t$  is unbounded, growing larger with longer in-the-wild sequences, making it unstable for a diffusion model to learn directly. We instead model the velocity  ${}^1\mathbf{v}_t = {}^1\mathbf{r}_t - {}^1\mathbf{r}_{t-1}$ . The world-space mesh can be recovered using  ${}^1\mathbf{X}_t = {}^1\mathbf{P}_t + \sum_{i=1}^t {}^1\mathbf{v}_i$ . Our world-space diffusion model generates  $({}^t\mathbf{P}_t, {}^t\mathbf{v}_t)$ . For brevity, we still use  $\mathbf{X}$  to denote the input and output of our diffusion models in the following sections.

#### 3.2. Camera-space diffusion

We generate camera-space human motion  $\mathbf{C}$  from video inputs. First, we extract two types of features: dense keypoints and image features. For each subject, we detect dense keypoints  $\mathbf{L}_t \in \mathbb{R}^{V \times 3}$  (homogeneous coordinates) using a model similar to recent dense keypoint methods [12, 53]. These dense keypoints have one-to-one correspondences with the 3D vertices on our sparse mesh. Instead of ingesting the keypoints’ 2D coordinates directly, we propose to convert them to ray directions using the camera intrinsics  $\mathbf{K}_t$ . We then encode each ray using a positional embedding function  $\gamma$  [52] and flatten the results, before processing them with an MLP. For invisible keypoints, we replace their embeddings with a learnable null embedding. This design implicitly encodes camera intrinsics, which is important for reconstruction accuracy [4, 15, 40]:

$$\begin{aligned} \mathbf{E}_t &= \gamma(\mathbf{K}_t^{-1} \cdot \mathbf{L}_t) \\ \mathbf{f}_t^{\text{kpt}} &= \text{MLP}(\text{vec}(\mathbf{E}_t)) \\ \mathbf{f}_t^{\text{img}} &= \text{Encoder}(\mathbf{I}_t) \\ \mathbf{f}_t &= \mathbf{f}_t^{\text{kpt}} + \mathbf{f}_t^{\text{img}}, \end{aligned} \quad (4)$$

where  $\text{vec}$  is the vectorization (flatten) operator. To extract image features, we input each frame  $\mathbf{I}_t$  to an image encoder to get  $\mathbf{f}_t^{\text{img}}$ . Finally, the two features are summed to get the final per-frame features  $\mathbf{f}_t$ .

The camera-space motion diffusion,  $\mathcal{D}_{\text{cam}}$ , takes this sequence of tokens  $\mathbf{f}_{1:T}$  as conditioning and generates motion  $\mathbf{C}$ . It uses a standard DiT architecture [55], where conditions  $\mathbf{f}_{1:T}$  are concatenated with noisy input  $\mathbf{C}_\tau$  along the feature dimension, and processed with blocks of self-attention to predict the clean output  $\mathbf{C}$ :

$$\mathbf{C} = \mathcal{D}_{\text{cam}}(\mathbf{C}_\tau, \tau, \mathbf{f}_{1:T}), \quad (5)$$

where  $\tau \in \{1, \dots, T\}$  is the diffusion time step [23].

We make a few improvements to the standard DiT to allow inference on longer sequences. First, we use relative positional embedding RoPE [66] on the input sequence. Second, we apply windowed attention to the sequence via masking. Consequently, tokens at each time step only attend to a local temporal neighborhood. At inference, our

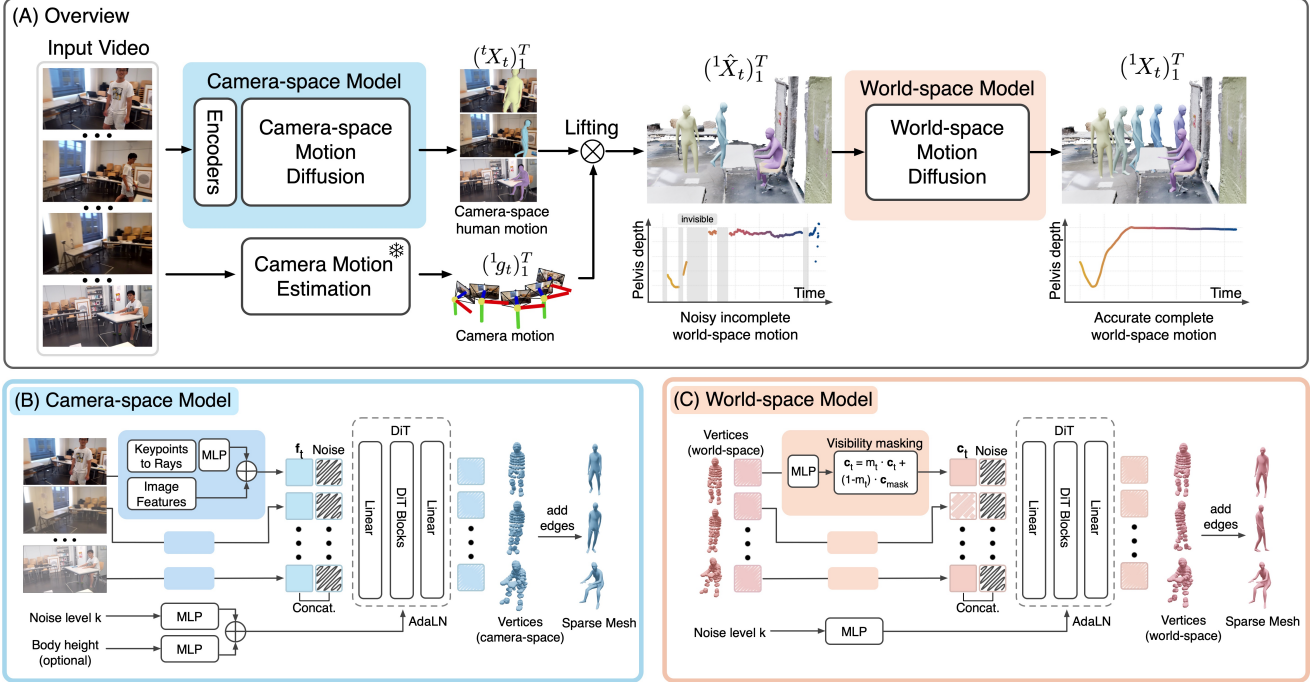


Figure 2. **Method overview.** (A) In the first stage, our camera-space model encodes video features and generates camera-space human motion. This motion is lifted to the world coordinates using estimated camera poses, becoming the initial proposal for world-space human motion. Some predictions are missing due to subject out of frame. In the second stage, the world-space model encodes the noisy world-space motion and generates globally consistent world-space motion. Plots at the bottom visualize the pelvis depth in the world coordinates. (B) Camera-space model architecture. (C) World-space model architecture.

model processes videos with thousands of frames without having to chunk.

**Height conditioning.** As illustrated in Fig. 3, height of the human body remains a large source of ambiguity despite the increasing amount of synthetic training data. However, this information is readily available in many applications. Therefore, we train our model to incorporate this information when it’s available. We show in experiments that learning to condition on height largely improves metric accuracy. To condition the model, we encode height (in meters) using an MLP and add it to the diffusion time step embedding. If height information is unavailable, we substitute the encoding with a learned null token [38].

### 3.3. World-space diffusion

We generate globally consistent world-space motion from the initial noisy proposal (Eq. 3) using our world-space motion diffusion model  $\mathcal{D}_{\text{world}}$ .  $\mathcal{D}_{\text{world}}$  uses the same DiT architecture (see Sec. 3.2), but takes the noisy lifted motion as conditioning. We encode  ${}^1\hat{X}_t$  with an MLP to get the condition  $c_t$  for each frame,

$$\begin{aligned} c_t &= \text{MLP}(\text{vec}({}^1\hat{X}_t)), \\ \mathbf{W} &= \mathcal{D}_{\text{world}}(\mathbf{W}_\tau, \tau, c_{1:T}). \end{aligned} \quad (6)$$

**Masked modeling.** To enable  $\mathcal{D}_{\text{world}}$  to generate plausible

motion when the subject is unobservable, we incorporate temporal masking in the training. Specifically,  $c_t$  is randomly replaced with a learnable mask token during training, to simulate no visibility at time  $t$ . At inference, the visibility token can be toggled and is determined by the number of confident keypoints.

### 3.4. Guided sampling

While our dual models produce accurate motion, the world-space model’s reliance on root velocity introduces two specific challenges that we address with test-time guided sampling. The first challenge is temporal drift. Because the world-space model outputs root velocities, integrating these velocities over time accumulates errors. This drift, while often minor, is observable as both 2D reprojection error and 3D misalignment with the scene, as visualized in Figure 4 (right).

The second challenge arises during long-range occlusions, when a person is unobservable for an extended period (e.g., from frame  $i$  to  $j$ ). While our world-space model can generate plausible connecting motion, it is not conditioned on the person’s absolute reappearance position. As a result, the integrated velocity  $\sum {}^1\mathbf{v}_{i:j}$  may produce a trajectory that does not land at the correct destination, as visualized in Figure 4 (left).

To address both issues, we introduce two test-time guid-

ance terms that steer the sampling trajectory during inference. The first is a 2D reprojection guidance

$$\mathcal{L}_{\text{repro}} = \sum_{t=1}^T \|\mathbf{L}_t - \mathbf{K}_t \cdot \mathbf{g}_t^{-1}({}^1\mathbf{X}_t)\|, \quad (7)$$

where  $\mathbf{L}_t$  are the detected 2D dense landmarks and  $\mathbf{g}_t^{-1}$  is the inverse camera pose. This loss encourages the world-space motion to align with the original video, to minimize temporal drift.

The second guidance is a displacement guidance, applied specifically during long occlusions (e.g. >2 seconds),

$$\mathcal{L}_{\text{disp}} = \sum_{(i,j) \in \text{Occ}} \left\| ({}^1\hat{\mathbf{r}}_j - {}^1\hat{\mathbf{r}}_i) - \sum_{t=i}^j {}^1\mathbf{v}_t \right\|, \quad (8)$$

where Occ is the set of long-occlusion segments. This loss ensures that the total displacement from the integrated root velocities matches the displacement between the human’s last visible position ( ${}^1\hat{\mathbf{r}}_i$ ) and first reappearance position ( ${}^1\hat{\mathbf{r}}_j$ ). These world-space positions are estimated by lifting the camera-space root position  ${}^1\hat{\mathbf{r}}_t = g_t({}^t\mathbf{r}_t)$ .

We implement these guidance objectives as  $x_0$ -guidance during DDIM sampling [64]. At each diffusion step, we compute the guidance gradient with respect to the predicted clean sample  $\hat{x}_0$  and use it to update  $\hat{x}_0$  before applying the standard DDIM update [3]. This approach is efficient as it avoids differentiating through the diffusion network [84].

### 3.5. Conversion to SMPLX

Prior work demonstrates regressing mesh vertices for individual frames [22, 34, 41], while our method generates vertices for the entire motion sequence. We convert the outputs to a parametric model for compactness and direct comparison with prior work.

We train an iterative MLP to convert our mesh to SMPLX parameters, avoiding the slow optimization-based conversion. This converter is inspired by learned optimization [11, 63, 86]. At each iteration, we compute the 3D errors between our sparse mesh vertices and the correspondences on the SMPLX mesh. The network takes the errors as input and predicts an update to the SMPLX parameters. Full details are in the supplementary material.

### 3.6. Training

**Training losses.** We train our camera-space and the world-space models separately. We train the camera-space model with a simple loss function

$$\mathcal{L}_{\text{Camera-space}} = \mathcal{L}_{\text{vertices}} + \mathcal{L}_{\text{position}} + \mathcal{L}_{\text{joints}},$$

where  $\mathcal{L}_{\text{vertices}}$ ,  $\mathcal{L}_{\text{position}}$ , and  $\mathcal{L}_{\text{joints}}$  are L1 losses on the predicted mesh vertices ( $P$ ), root position ( $r$ ), and derived joint positions, respectively all in the camera space.

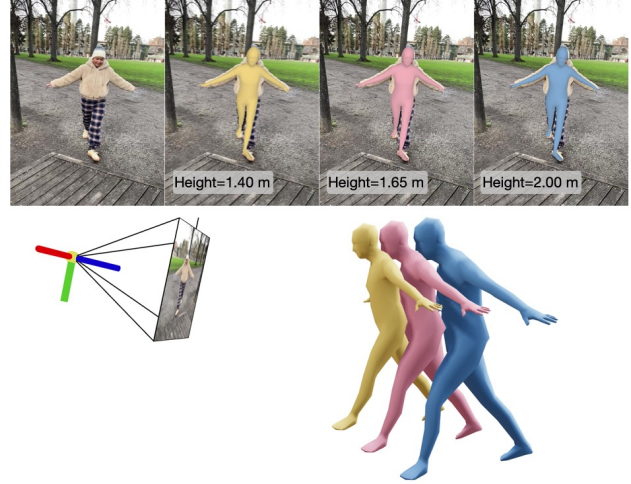


Figure 3. **Height conditioning.** Our camera-space model can generate predictions based on input body heights. As shown at the bottom row, height impacts distance from camera and thus plays an important role in world-space accuracy.

After training, the model weights are frozen. We then use it in the training loop of the world-space model. The loss for the world-space model is defined as

$$\mathcal{L}_{\text{World-space}} = \mathcal{L}_{\text{vertices}} + \mathcal{L}_{\text{velocity}} + \mathcal{L}_{\text{contact}},$$

which includes an L1 loss on the vertices and root velocity in the world space.

The  $\mathcal{L}_{\text{contact}}$  term is important for reducing foot-skating artifacts. Prior works predict contact labels for a post-hoc foot-locking step [61, 77]. In contrast, we reinforce physically-plausible contact during training. We define this loss as the L1 error on the world-space foot vertices, applied only on frames where the foot is in contact with the ground:

$$\mathcal{L}_{\text{contact}} = \frac{1}{|S|} \sum_{t \in S} \|{}^1X_{t,\text{foot}} - {}^1X_{t,\text{foot}}^*\|,$$

where  ${}^1X_{t,\text{foot}}$  are the predicted foot vertices at  $t$ ,  ${}^1X_{t,\text{foot}}^*$  is the corresponding ground truth, and  $S$  is the set of frames where the foot is in contact with the ground.

**Implementation details.** We adopt the 595-vertex LOD6 sparse mesh from MHR [16]. This specific level of detail effectively captures human pose and shape, while the low vertex count makes training more efficient.

For our camera-space model, we use the frozen image encoder from PromptHMR [77]. The encoder from HMR2 [19] has a similar effect. We use the dense keypoint detection model from SAM 3D Body [81].

We trained our motion diffusion models separately with AdamW for one million steps, with a learning rate of  $10^{-4}$  and an effective batch size of 256. During training, the sequence length  $T$  is set to 120. Full implementation details are in the supplementary material.

Models	EMDB (24)			RICH (24)			
	PA-MPJPE	MPJPE	PVE	PA-MPJPE	MPJPE	PVE	
per-frame	HMR2.0 [19]	61.5	97.8	120.0	60.7	98.3	120.8
	ReFit [14]	58.6	88.0	104.5	47.9	80.7	92.9
	CameraHMR [53]	43.3	70.2	81.7	<b>34.0</b>	55.7	64.4
	NLF [60]	41.2	69.6	82.4	-	-	-
	PromptHMR [77]	<b>41.0</b>	71.7	84.5	37.3	56.6	65.5
temporal	WHAM [62]	52.0	81.6	96.9	44.3	80.0	91.2
	TRAM [76]	45.7	74.4	86.6	-	-	-
	GVHMR [61]	44.5	74.2	85.9	39.5	66.0	74.4
	GENMO [38]	42.5	73.0	84.8	39.1	66.8	75.4
	<b>Ours</b>	41.8	<u>67.1</u>	<u>78.2</u>	<u>34.8</u>	<u>51.4</u>	<u>58.9</u>
<b>Ours (w/ height)</b>	<u>41.7</u>	<b>59.5</b>	<b>70.4</b>	35.0	<b>48.0</b>	<b>55.2</b>	

Table 1. **Camera-space reconstruction** on EMDB [28] and RICH [24], with the number of joints in parenthesis. Our method does not use test-time flip augmentation. All metrics are in *mm*.

**Datasets.** We trained our two motion diffusion models with common datasets. The camera-space model is trained with AMASS [49], BEDLAM [5], 3DPW [75] and Goliath [50]. The world-space model is trained with AMASS [49] and BEDLAM [5]. We trained the dense keypoint detection model on BEDLAM. On AMASS, we simulate camera motion following WHAM [62].

## 4. Experiments

We evaluate DuoMo on camera-space reconstruction, world-space reconstruction, and motion quality. To compare with prior methods, we use our converter to transform our sparse meshes to SMPLX meshes and joints to compute accuracy. Our method uses ground truth camera intrinsics for all evaluations.

### 4.1. Camera-space reconstruction

We first evaluate our camera-space model’s accuracy on the EMDB [28] and RICH [24] datasets. As shown in Table 1, our method achieves new state-of-the-art performance.

We find this accuracy is impacted by the inherent scale ambiguity of monocular reconstruction. This is visualized in Figure 3, which shows that multiple 3D reconstructions can align perfectly with the 2D image evidence while having different body heights and distances from the camera.

Our height-conditioning mechanism resolves this ambiguity with additional information. Conditioning on ground-truth subject height during inference yields a 10% improvement on both MPJPE and PVE. This result demonstrates that resolving body scale is a crucial step for accurately “lifting” the motion into a consistent world space.

### 4.2. World-space reconstruction

We evaluate our world-space model’s accuracy using the EMDB [28] and RICH [24] datasets. For a fair comparison on EMDB, we use the camera motion provided by

Models	Visible segment		Full segment			
	W-MPJPE	RTE	W-MPJPE	RTE	W-MPJPE-Occ	RTE-Occ
PHMR [77]	271.1	2.3	357.2	3.3	885.0	12.0
GVHMR [61]	189.1	3.9	209.4	3.9	384.1	6.1
Cam-model + Lifting	95.3	<b>0.7</b>	174.2	1.9	688.1	10.4
DuoMo	99.7	1.5	109.3	1.6	193.1	2.6
DuoMo w/ guidance	<b>90.4</b>	1.0	<b>101.3</b>	<b>1.1</b>	<b>175.4</b>	<b>1.7</b>

Table 2. **Robust reconstruction** on the Egobody [88], evaluating both visible and invisible segments (e.g. person out of frame). All methods use ground truth camera poses in this evaluation.

Methods	WA-MPJPE	W-MPJPE	RTE	Jitter	Foot Skating
World-space model (one stage)	153.5	445.1	6.7	<u>9.1</u>	<u>4.8</u>
Cam-space model + Lifting	<u>67.0</u>	<u>180.2</u>	<u>1.3</u>	32.6	9.2
DuoMo	<b>66.0</b>	<b>167.1</b>	<b>1.1</b>	<b>8.7</b>	<b>3.7</b>

Table 3. **Ablation for DuoMo design** on EMDB [28]. DuoMo has higher accuracy and motion quality than using only one model.

TRAM [76], as most methods are sensitive to camera pose accuracy. On RICH, we use the static camera poses.

We evaluate world-space motion using: WA-MPJPE (joint accuracy on Procrustes-aligned 100-frame segments); W-MPJPE (joint accuracy on 100-frame segments aligned only at the first two frames); and RTE (root trajectory position error in %). Full details in the supplementary.

As shown in Table 4, DuoMo demonstrates significant improvements in both 3D accuracy and motion quality. Our W-MPJPE is 16% lower on EMDB and 30% lower on RICH than the second best method. At the same time, we have high motion quality, with low foot-sliding score comparable to GVHMR which requires post-hoc foot-locking.

We show a qualitative comparison in Figure 5. Compared to others [61, 77], our results have higher scene consistency and less drifting. We attribute this performance gain to our dual model design, which we analyze in our ablation studies 4.4.

### 4.3. Generative reconstruction

We evaluate the robustness and generative capabilities of DuoMo on the challenging egocentric subset of the Egobody [88] dataset. These sequences are captured by a moving HoloLens featuring moving subjects in indoor environments. The videos are shaky, with subjects frequently truncated and out of frame. For this experiment, we use the tracked camera motion from HoloLens.

We establish two evaluation tracks. **Visible reconstruction** evaluates accuracy only on the frames where the subject is visible. **Full-sequence reconstruction** evaluates accuracy over the entire sequence, including when the subject is out of frame. For this track, we report metrics on the full sequence and also on the occluded segments specifically (W-MPJPE-Occ and RTE-Occ).

As shown in Table 2, DuoMo demonstrates high accuracy and robustness. A key comparison is against our

Models	EMDB (24)					RICH (24)				
	WA-MPJPE	W-MPJPE	RTE	Jitter	Foot-sliding	WA-MPJPE	W-MPJPE	RTE	Jitter	Foot-sliding
TRACE [68]	529.0	1702.3	17.7	2987.6	370.7	238.1	925.4	610.4	1578.6	230.7
GLAMR [83]	280.8	726.6	11.4	46.3	20.7	129.4	236.2	3.8	49.7	18.1
SLAHMR [82]	326.9	776.1	10.2	31.3	14.5	98.1	186.4	28.9	34.3	5.1
WHAM [62]	135.6	354.8	6.0	22.5	4.4	109.9	184.6	4.1	19.7	3.3
GVHMR [61]	111.0	276.5	2.0	16.7	<b>3.5</b>	78.8	126.3	2.4	12.8	<b>3.0</b>
TRAM [76]	76.4	222.4	1.4	18.1	11.0	–	–	–	–	–
GENMO [38]	74.3	202.1	1.2	17.8	8.8	75.3	118.6	1.9	15.0	6.7
<b>Ours</b>	67.6	171.6	1.2	8.7	3.7	53.6	80.8	1.3	5.3	3.1
<b>Ours (w/ height)</b>	<b>66.0</b>	<b>167.1</b>	<b>1.1</b>	<b>8.7</b>	3.7	<b>53.5</b>	<b>80.4</b>	<b>1.3</b>	<b>5.2</b>	3.1

Table 4. **World-space reconstruction** on the EMDB [28] and RICH [24] datasets. We do not use test-time flip augmentation. Our method uses the same estimated camera motion as TRAM [76] and GENMO [38], providing a meaningful comparison.

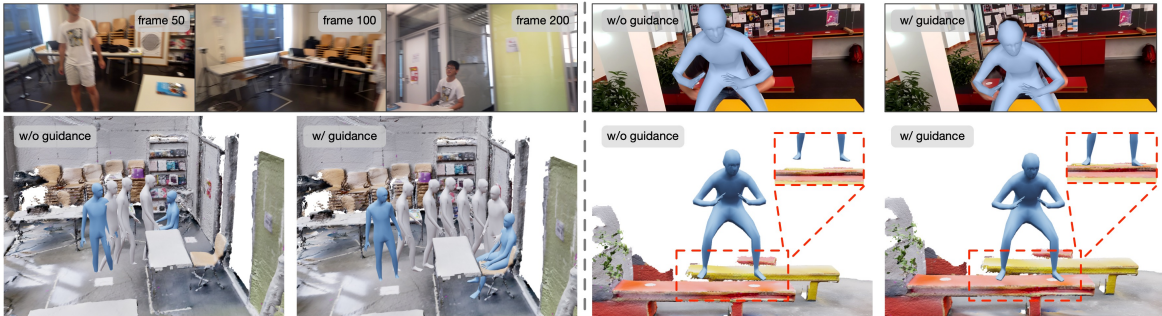


Figure 4. **Guided sampling** on Egobody [44]. Our proposed guidances correct for drifting and improve world-space trajectory accuracy.

DuoMo w/	WA-MPJPE	W-MPJPE	RTE	Jitter	Foot Skating
World-Model-SMPL	70.1	182.5	1.3	<b>7.4</b>	4.8
World-Model-Mesh	<b>65.7</b>	<b>164.8</b>	<b>1.1</b>	8.5	<b>3.8</b>

Table 5. **Ablation for motion representation** on EMDB [28]. Directly generating sparse mesh is very competitive in terms of motion reconstruction accuracy.

camera-space model+lifting baseline. The baseline is unable to generate plausible world-space motion during occlusions, showing high W-MPJPE-Occ error. In contrast, DuoMo’s world-space modeling provides a generative prior to complete the motion, as evidenced by the gains on the full-sequence metrics.

Furthermore, these results underscore the importance of guided sampling. While the generative model can produce plausible motion, it is not sufficient for accurate reconstruction under occlusion. The generative process must also consider the human’s reappearance. Our 2D reprojection and displacement guidance terms enforce this, improving RTE and RTE-Occ. A qualitative comparison in Figure 4 visualizes this effect.

#### 4.4. Ablation studies

**Dual priors.** We perform ablation studies to validate the core technical choices. We first analyze the dual models in Table 3. The direct lifting approach (Cam-model+Lifting) achieves good accuracy but its motion quality is poor with

high jitter and foot skating. Conversely, we created a one-stage world-space model only baseline. This model learns a stronger world-space motion prior and produces plausible motion but has subpar accuracy. This highlights the difficulty of solving 2D-to-3D lifting and global consistency simultaneously. Prior works that attempt this often rely on stronger inductive biases [61, 62]. Our DuoMo factorization achieves the best of both worlds.

**Representation.** We freeze our camera-space model and train a new world-space model that outputs SMPLX parameters. We adapt the loss setup from prior works [19], adding our  $\mathcal{L}_{\text{contact}}$  term for a fair comparison. As shown in Table 5, our sparse mesh approach is highly competitive. This is a promising outcome, as it suggests our architecture can be extended to learn motion models for other categories directly from surface supervision without parametric models.

**Camera estimation error.** We analyze the critical role of camera pose accuracy in world-space human reconstruction. First, we establish a realistic noise profile by comparing TRAM’s camera estimation against the iPhone-tracked “ground truth” camera poses on EMDB [28]. We then model this error as accumulating, per-frame Gaussian noise on the Lie algebra (for rotation) and Euclidean coordinates (for translation) to simulate SLAM drift. We apply this noise at increasing intensities to the ground truth camera. We sample 10 camera trajectories per-level per-sequence, and average our human reconstruction accuracy.

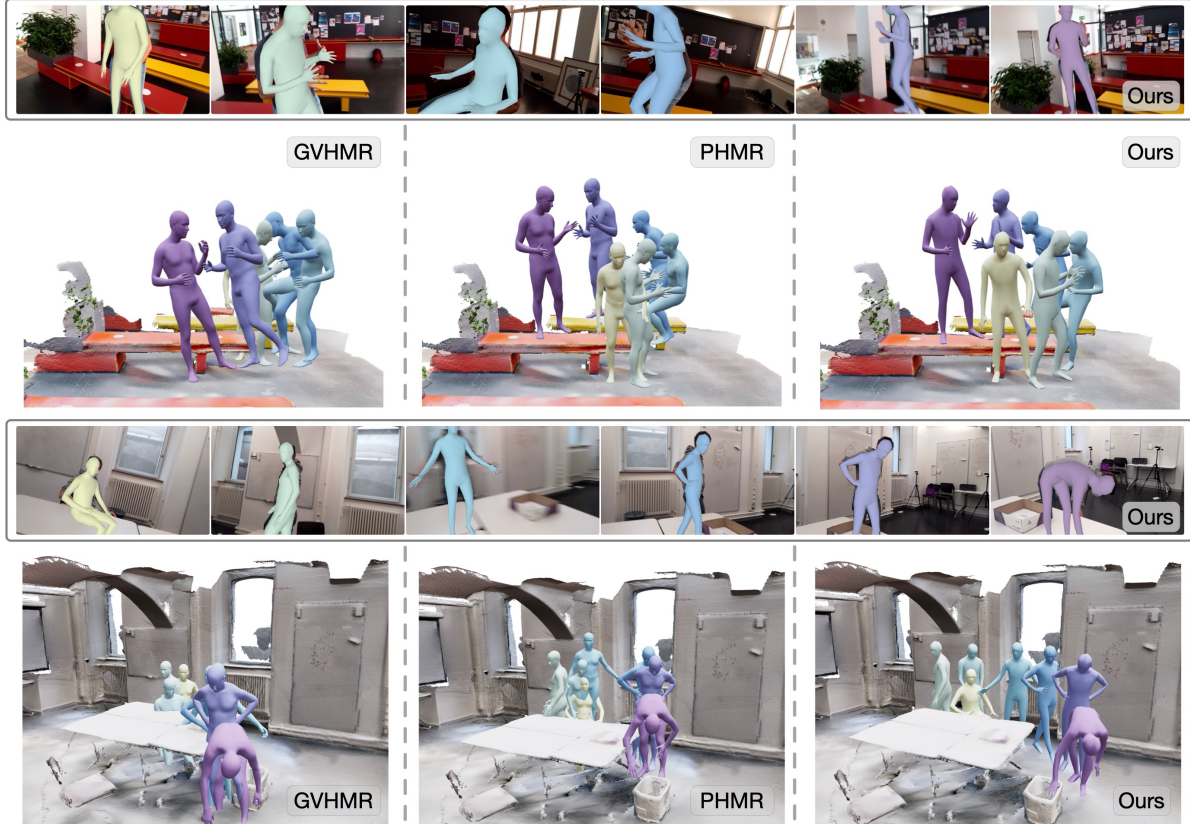


Figure 5. **Qualitative comparison** on Egobody [88]. All methods use the ground truth camera poses. We observe that results from GVHMR [61] are smooth but drift under shaky camera motion. PromptHMR [77] has better position accuracy but is not robust to occlusion and depth ambiguity. Our results show both accuracy and robustness.

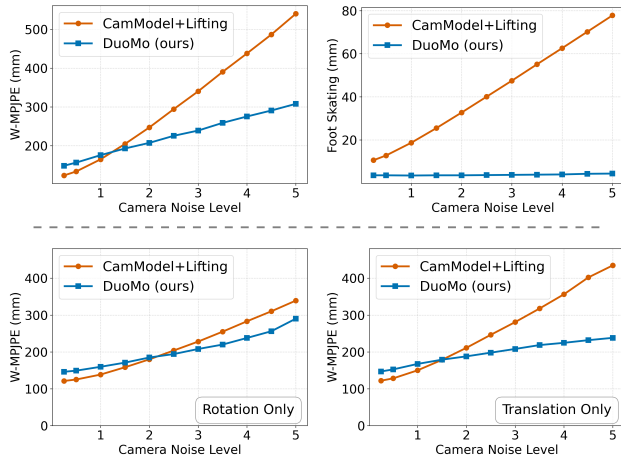


Figure 6. **Impact of camera error.** Comparison of methods under different camera motion noise levels.

Figure 6 (top) shows that the Cam-model+Lifting baseline, while achieving a low W-MPJPE at near-zero noise, is very brittle; its accuracy degrades rapidly, and its foot-skating (FS) score explodes as noise increases. In contrast, DuoMo is more robust. Its W-MPJPE degrades gracefully, and its foot-skating remains minimal across all noise levels.

This demonstrates that the world-space model acts as a generative regularizer: it sacrifices a small amount of per-frame fidelity at low noise to gain robustness and maintain physical plausibility. The bottom plot further isolates this effect, by only applying rotation noise or translation noise to the camera trajectory. It shows that while the Cam-model+Lifting baseline’s error degrades rapidly from translation noise, DuoMo’s accuracy is more stable.

**Speed.** On an H200, a 20s video (30FPS) takes 2s, 3s, 30s, and 1.5s for extracting keypoints, dense keypoints, image features, and diffusion respectively. We discuss limitations in the supplementary.

## 5. Conclusion

We presented DuoMo, a two-stage diffusion method for world-space human motion reconstruction. Our approach achieves robustness and generality by decoupling the problem into a camera-space estimation stage and a world-space refinement stage that operates in per-video coordinate systems. Furthermore, our architecture generates the motion of mesh vertices directly. Experiments validate that DuoMo achieves state-of-the-art performance.

## References

- [1] Arthur Allshire, Hongsuk Choi, Junyi Zhang, David McAllister, Anthony Zhang, Chung Min Kim, Trevor Darrell, Pieter Abbeel, Jitendra Malik, and Angjoo Kanazawa. Visual imitation enables contextual humanoid control. *arXiv preprint arXiv:2505.03729*, 2025. 2
- [2] Anurag Arnab, Carl Doersch, and Andrew Zisserman. Exploiting temporal context for 3D human pose estimation in the wild. In *Proceedings of the IEEE/CVF Conference on Computer Vision and Pattern Recognition*, pages 3395–3404, 2019. 2
- [3] Arpit Bansal, Hong-Min Chu, Avi Schwarzschild, Soumyadip Sengupta, Micah Goldblum, Jonas Geiping, and Tom Goldstein. Universal guidance for diffusion models. In *Proceedings of the IEEE/CVF conference on computer vision and pattern recognition*, pages 843–852, 2023. 5
- [4] Fabien Baradel, Matthieu Armando, Salma Galaoui, Romain Brégier, Philippe Weinzaepfel, Grégory Rogez, and Thomas Lucas. Multi-HMR: Multi-person whole-body human mesh recovery in a single shot. *European Conference on Computer Vision*, 2024. 2, 3
- [5] Michael J Black, Priyanka Patel, Joachim Tesch, and Jintong Yang. BEDLAM: A synthetic dataset of bodies exhibiting detailed lifelike animated motion. In *Proceedings of the IEEE/CVF Conference on Computer Vision and Pattern Recognition*, pages 8726–8737, 2023. 2, 6, 13, 14
- [6] Randolph Blake and Maggie Shiffrar. Perception of human motion. *Annu. Rev. Psychol.*, 58(1):47–73, 2007. 1
- [7] Federica Bogo, Angjoo Kanazawa, Christoph Lassner, Peter Gehler, Javier Romero, and Michael J Black. Keep it SMPL: Automatic estimation of 3D human pose and shape from a single image. In *European Conference on Computer Vision*, pages 561–578. Springer, 2016. 2
- [8] Xin Chen, Biao Jiang, Wen Liu, Zilong Huang, Bin Fu, Tao Chen, and Gang Yu. Executing your commands via motion diffusion in latent space. In *Proceedings of the IEEE/CVF conference on computer vision and pattern recognition*, pages 18000–18010, 2023. 3
- [9] Yue Chen, Xingyu Chen, Yuxuan Xue, Anpei Chen, Yuliang Xiu, and Gerard Pons-Moll. Human3r: Everyone everywhere all at once. *arXiv preprint arXiv:2510.06219*, 2025. 2
- [10] Hongsuk Choi, Gyeongsik Moon, Ju Yong Chang, and Kyoung Mu Lee. Beyond static features for temporally consistent 3D human pose and shape from a video. In *Proceedings of the IEEE/CVF Conference on Computer Vision and Pattern Recognition*, pages 1964–1973, 2021. 2
- [11] Vasileios Choutas, Federica Bogo, Jingjing Shen, and Julien Valentin. Learning to fit morphable models. In *European Conference on Computer Vision*, pages 160–179. Springer, 2022. 5, 13
- [12] Hanz Cuevas-Velasquez, Anastasios Yiannakidis, Soyong Shin, Giorgio Becherini, Markus Höschle, Joachim Tesch, Taylor Obersat, Tsvetelina Alexiadis, and Michael J Black. Mamma: Markerless & automatic multi-person motion action capture. *arXiv preprint arXiv:2506.13040*, 2025. 3
- [13] Alexey Dosovitskiy, Lucas Beyer, Alexander Kolesnikov, Dirk Weissenborn, Xiaohua Zhai, Thomas Unterthiner, Mostafa Dehghani, Matthias Minderer, Georg Heigold, Sylvain Gelly, et al. An image is worth 16x16 words: Transformers for image recognition at scale. *arXiv preprint arXiv:2010.11929*, 2020. 2
- [14] Sai Kumar Dwivedi, Yu Sun, Priyanka Patel, Yao Feng, and Michael J Black. TokenHMR: Advancing human mesh recovery with a tokenized pose representation. In *Proceedings of the IEEE/CVF Conference on Computer Vision and Pattern Recognition*, pages 1323–1333, 2024. 3, 6
- [15] Qiao Feng, Yiming Huang, Yufu Wang, Jiatao Gu, and Lingjie Liu. Physmr: Learning humanoid control policies from vision for physically plausible human motion reconstruction. *arXiv preprint arXiv:2510.02566*, 2025. 3
- [16] Aaron Ferguson, Ahmed AA Osman, Berta Bescos, Carsten Stoll, Chris Twigg, Christoph Lassner, David Otte, Eric Vignola, Fabian Prada, Federica Bogo, et al. Mhr: Momentum human rig. *arXiv preprint arXiv:2511.15586*, 2025. 5, 13
- [17] Guérolé Fiche, Simon Leglaive, Xavier Alameda-Pineda, and Francesc Moreno-Noguer. Mega: Masked generative auto-encoder for human mesh recovery. In *Proceedings of the Computer Vision and Pattern Recognition Conference*, pages 5366–5378, 2025. 15
- [18] Jing Gao, Ce Zheng, Laszlo A Jeni, and Zackory Erickson. Disrt-in-bed: diffusion-based sim-to-real transfer framework for in-bed human mesh recovery. In *Proceedings of the IEEE/CVF Conference on Computer Vision and Pattern Recognition*, pages 1829–1838, 2025. 3
- [19] Shubham Goel, Georgios Pavlakos, Jathushan Rajasegaran, Angjoo Kanazawa, and Jitendra Malik. Reconstructing and tracking humans with transformers. *Proceedings of the IEEE/CVF International Conference on Computer Vision*, 2023. 2, 5, 6, 7
- [20] Vladimir Guzov, Aymen Mir, Torsten Sattler, and Gerard Pons-Moll. Human positioning system (HPS): 3D human pose estimation and self-localization in large scenes from body-mounted sensors. In *Proceedings of the IEEE/CVF Conference on Computer Vision and Pattern Recognition*, pages 4318–4329, 2021. 2
- [21] Mohamed Hassan, Duygu Ceylan, Ruben Villegas, Jun Saito, Jimei Yang, Yi Zhou, and Michael J Black. Stochastic scene-aware motion prediction. In *Proceedings of the IEEE/CVF International Conference on Computer Vision*, pages 11374–11384, 2021. 3
- [22] Hsuan-I Ho, Chen Guo, Po-Chen Wu, Ivan Shugurov, Chengcheng Tang, Abhay Mittal, Sizhe An, Manuel Kaufmann, and Linguang Zhang. Phd: Personalized 3d human body fitting with point diffusion. In *Proceedings of the IEEE/CVF International Conference on Computer Vision*, pages 7526–7537, 2025. 3, 5
- [23] Jonathan Ho, Ajay Jain, and Pieter Abbeel. Denoising diffusion probabilistic models. *Advances in neural information processing systems*, 33:6840–6851, 2020. 2, 3, 14
- [24] Chun-Hao P Huang, Hongwei Yi, Markus Höschle, Matvey Safroshkin, Tsvetelina Alexiadis, Senya Polikovsky, Daniel Scharstein, and Michael J Black. Capturing and inferring

- dense full-body human-scene contact. In *Proceedings of the IEEE/CVF Conference on Computer Vision and Pattern Recognition*, pages 13274–13285, 2022. 2, 6, 7
- [25] Chun-Hao P Huang, Hongwei Yi, Markus Hoshle, Matvey Safroshkin, Tsvetelina Alexiadis, Senya Polikovsky, Daniel Scharstein, and Michael J Black. Capturing and inferring dense full-body human-scene contact. In *Proceedings of the IEEE/CVF Conference on Computer Vision and Pattern Recognition*, pages 13274–13285, 2022. 2
- [26] Yinghao Huang, Federica Bogo, Christoph Lassner, Angjoo Kanazawa, Peter V Gehler, Javier Romero, Ijaz Akhter, and Michael J Black. Towards accurate marker-less human shape and pose estimation over time. In *International Conference on 3D Vision*, pages 421–430. IEEE, 2017. 2
- [27] Angjoo Kanazawa, Michael J Black, David W Jacobs, and Jitendra Malik. End-to-end recovery of human shape and pose. In *Proceedings of the IEEE/CVF Conference on Computer Vision and Pattern Recognition*, pages 7122–7131, 2018. 2
- [28] Manuel Kaufmann, Jie Song, Chen Guo, Kaiyue Shen, Tianjian Jiang, Chengcheng Tang, Juan José Zárate, and Otmar Hilliges. EMDb: The electromagnetic database of global 3d human pose and shape in the wild. In *Proceedings of the IEEE/CVF International Conference on Computer Vision*, pages 14632–14643, 2023. 2, 6, 7, 13, 14
- [29] Manuel Kaufmann, Jie Song, Chen Guo, Kaiyue Shen, Tianjian Jiang, Chengcheng Tang, Juan José Zárate, and Otmar Hilliges. Emdb: The electromagnetic database of global 3d human pose and shape in the wild. In *Proceedings of the IEEE/CVF International Conference on Computer Vision*, pages 14632–14643, 2023. 2
- [30] Diederik P Kingma and Max Welling. Auto-encoding variational bayes. *arXiv preprint arXiv:1312.6114*, 2013. 2
- [31] Muhammed Kocabas, Nikos Athanasiou, and Michael J Black. VIBE: Video inference for human body pose and shape estimation. In *Proceedings of the IEEE/CVF Conference on Computer Vision and Pattern Recognition*, pages 5253–5263, 2020. 2
- [32] Muhammed Kocabas, Chun-Hao P Huang, Otmar Hilliges, and Michael J Black. PARE: Part attention regressor for 3D human body estimation. In *Proceedings of the IEEE/CVF International Conference on Computer Vision*, pages 11127–11137, 2021. 2
- [33] Nikos Kolotouros, Georgios Pavlakos, Michael J Black, and Kostas Daniilidis. Learning to reconstruct 3D human pose and shape via model-fitting in the loop. In *Proceedings of the IEEE/CVF International Conference on Computer Vision*, pages 2252–2261, 2019. 2
- [34] Nikos Kolotouros, Georgios Pavlakos, and Kostas Daniilidis. Convolutional mesh regression for single-image human shape reconstruction. In *Proceedings of the IEEE/CVF Conference on Computer Vision and Pattern Recognition*, pages 4501–4510, 2019. 5
- [35] Nikos Kolotouros, Georgios Pavlakos, Dinesh Jayaraman, and Kostas Daniilidis. Probabilistic modeling for human mesh recovery. In *Proceedings of the IEEE/CVF International Conference on Computer Vision*, pages 11605–11614, 2021. 3
- [36] Jiefeng Li, Chao Xu, Zhicun Chen, Siyuan Bian, Lixin Yang, and Cewu Lu. HybrIK: A hybrid analytical-neural inverse kinematics solution for 3D human pose and shape estimation. In *Proceedings of the IEEE/CVF Conference on Computer Vision and Pattern Recognition*, pages 3383–3393, 2021. 2
- [37] Jiefeng Li, Siyuan Bian, Chao Xu, Gang Liu, Gang Yu, and Cewu Lu. D&D: Learning human dynamics from dynamic camera. In *European Conference on Computer Vision*, pages 479–496. Springer, 2022. 2
- [38] Jiefeng Li, Jinkun Cao, Haotian Zhang, Davis Rempe, Jan Kautz, Umar Iqbal, and Ye Yuan. Genmo: A generalist model for human motion. *arXiv preprint arXiv:2505.01425*, 2025. 1, 2, 3, 4, 6, 7, 14
- [39] Ruilong Li, Shan Yang, David A Ross, and Angjoo Kanazawa. Ai choreographer: Music conditioned 3d dance generation with aist++. In *Proceedings of the IEEE/CVF international conference on computer vision*, pages 13401–13412, 2021. 3
- [40] Zhihao Li, Jianzhuang Liu, Zhensong Zhang, Songcen Xu, and Youliang Yan. CLIFF: Carrying location information in full frames into human pose and shape estimation. In *European Conference on Computer Vision*, pages 590–606. Springer, 2022. 2, 3
- [41] Kevin Lin, Lijuan Wang, and Zicheng Liu. End-to-end human pose and mesh reconstruction with transformers. In *Proceedings of the IEEE/CVF Conference on Computer Vision and Pattern Recognition*, pages 1954–1963, 2021. 5
- [42] Yuchen Lin, Chenguo Lin, Panwang Pan, Honglei Yan, Yiqiang Feng, Yadong Mu, and Katerina Fragkiadaki. Partcrafter: Structured 3d mesh generation via compositional latent diffusion transformers. *arXiv preprint arXiv:2506.05573*, 2025. 15
- [43] Haiyang Liu, Zihao Zhu, Giorgio Becherini, Yichen Peng, Mingyang Su, You Zhou, Xuefei Zhe, Naoya Iwamoto, Bo Zheng, and Michael J Black. Emage: Towards unified holistic co-speech gesture generation via expressive masked audio gesture modeling. In *Proceedings of the IEEE/CVF Conference on Computer Vision and Pattern Recognition*, pages 1144–1154, 2024. 3
- [44] Miao Liu, Dexin Yang, Yan Zhang, Zhaopeng Cui, James M Rehg, and Siyu Tang. 4D human body capture from egocentric video via 3D scene grounding. In *International Conference on 3D Vision*, pages 930–939. IEEE, 2021. 2, 7
- [45] Zhizheng Liu, Joe Lin, Wayne Wu, and Bolei Zhou. Joint optimization for 4d human-scene reconstruction in the wild. *arXiv preprint arXiv:2501.02158*, 2025. 2
- [46] Matthew Loper, Naureen Mahmood, Javier Romero, Gerard Pons-Moll, and Michael J Black. SMPL: A skinned multi-person linear model. *ACM TOG*, 34(6):1–16, 2015. 2, 13
- [47] Matthew Loper, Naureen Mahmood, Javier Romero, Gerard Pons-Moll, and Michael J Black. Smpl: A skinned multi-person linear model. In *Seminal Graphics Papers: Pushing the Boundaries, Volume 2*, pages 851–866. 2023. 2
- [48] Junzhe Lu, Jing Lin, Hongkun Dou, Ailing Zeng, Yue Deng, Xian Liu, Zhongang Cai, Lei Yang, Yulun Zhang, Haoqian Wang, et al. Dposer-x: Diffusion model as robust 3d whole-body human pose prior. In *Proceedings of the IEEE/CVF*

- International Conference on Computer Vision*, pages 9988–9997, 2025. 3
- [49] Naureen Mahmood, Nima Ghorbani, Nikolaus F Troje, Gerard Pons-Moll, and Michael J Black. AMASS: Archive of motion capture as surface shapes. In *Proceedings of the IEEE/CVF International Conference on Computer Vision*, pages 5442–5451, 2019. 2, 6, 13, 14
- [50] Julieta Martinez, Emily Kim, Javier Romero, Timur Bagautdinov, Shunsuke Saito, Shoou-I Yu, Stuart Anderson, Michael Zollhöfer, Te-Li Wang, Shaojie Bai, Chenghui Li, Shih-En Wei, Rohan Joshi, Wyatt Borsos, Tomas Simon, Jason Saragih, Paul Theodosis, Alexander Greene, Anjani Josyula, Silvio Mano Maeta, Andrew I. Jewett, Simon Venstain, Christopher Heilman, Yueh-Tung Chen, Sidi Fu, Mohamed Ezzeldin A. Elshaer, Tingfang Du, Longhua Wu, Shen-Chi Chen, Kai Kang, Michael Wu, Youssef Emad, Steven Longay, Ashley Brewer, Hitesh Shah, James Booth, Taylor Koska, Kayla Haidle, Matt Andromalos, Joanna Hsu, Thomas Dauer, Peter Selednik, Tim Godisart, Scott Ardisson, Matthew Cipperly, Ben Humberston, Lon Farr, Bob Hansen, Peihong Guo, Dave Braun, Steven Krenn, He Wen, Lucas Evans, Natalia Fadeeva, Matthew Stewart, Gabriel Schwartz, Divam Gupta, Gyeongsik Moon, Kaiwen Guo, Yuan Dong, Yichen Xu, Takaaki Shiratori, Fabian Prada, Bernardo R. Pires, Bo Peng, Julia Buffalini, Autumn Trimble, Kevyn McPhail, Melissa Schoeller, and Yaser Sheikh. Codec Avatar Studio: Paired Human Captures for Complete, Driveable, and Generalizable Avatars. *NeurIPS Track on Datasets and Benchmarks*, 2024. 6, 14
- [51] James V McConnell. *Understanding human behavior: An introduction to psychology*. Holt, Rinehart & Winston, 1974. 1
- [52] Ben Mildenhall, Pratul P Srinivasan, Matthew Tancik, Jonathan T Barron, Ravi Ramamoorthi, and Ren Ng. Nerf: Representing scenes as neural radiance fields for view synthesis. *Communications of the ACM*, 65(1):99–106, 2021. 3
- [53] Priyanka Patel and Michael J. Black. Camerahmr: Aligning people with perspective. *International Conference on 3D Vision (3DV)*, 2025. 2, 3, 6
- [54] Georgios Pavlakos, Vasileios Choutas, Nima Ghorbani, Timo Bolkart, Ahmed AA Osman, Dimitrios Tzionas, and Michael J Black. Expressive body capture: 3D hands, face, and body from a single image. In *Proceedings of the IEEE/CVF Conference on Computer Vision and Pattern Recognition*, pages 10975–10985, 2019. 2, 13
- [55] William Peebles and Saining Xie. Scalable diffusion models with transformers. In *Proceedings of the IEEE/CVF international conference on computer vision*, pages 4195–4205, 2023. 3, 14
- [56] Xue Bin Peng, Angjoo Kanazawa, Jitendra Malik, Pieter Abbeel, and Sergey Levine. Sfv: Reinforcement learning of physical skills from videos. *ACM Transactions On Graphics (TOG)*, 37(6):1–14, 2018. 1
- [57] Davis Rempe, Tolga Birdal, Aaron Hertzmann, Jimei Yang, Srinath Sridhar, and Leonidas J Guibas. HUMOR: 3D human motion model for robust pose estimation. In *Proceedings of the IEEE/CVF International Conference on Computer Vision*, pages 11488–11499, 2021. 2, 3
- [58] Robin Rombach, Andreas Blattmann, Dominik Lorenz, Patrick Esser, and Björn Ommer. High-resolution image synthesis with latent diffusion models. In *Proceedings of the IEEE/CVF conference on computer vision and pattern recognition*, pages 10684–10695, 2022. 15
- [59] Muhammad Usama Saleem, Ekkasit Pinyoanuntapong, Pu Wang, Hongfei Xue, Srijan Das, and Chen Chen. Genhmr: Generative human mesh recovery. In *Proceedings of the AAAI Conference on Artificial Intelligence*, pages 6749–6757, 2025. 3
- [60] István Sárádi and Gerard Pons-Moll. Neural localizer fields for continuous 3d human pose and shape estimation. *Advances in Neural Information Processing Systems*, 37: 140032–140065, 2024. 2, 6, 13
- [61] Zehong Shen, Huaijin Pi, Yan Xia, Zhi Cen, Sida Peng, Zechen Hu, Hujun Bao, Ruizhen Hu, and Xiaowei Zhou. World-grounded human motion recovery via gravity-view coordinates. In *SIGGRAPH Asia*, 2024. 1, 2, 5, 6, 7, 8
- [62] Soyong Shin, Juyong Kim, Eni Halilaj, and Michael J Black. WHAM: Reconstructing world-grounded humans with accurate 3D motion. *arXiv preprint arXiv:2312.07531*, 2023. 1, 2, 6, 7
- [63] Jie Song, Xu Chen, and Otmar Hilliges. Human body model fitting by learned gradient descent. In *European Conference on Computer Vision*. Springer, 2020. 5, 13
- [64] Jiaming Song, Chenlin Meng, and Stefano Ermon. Denoising diffusion implicit models. *arXiv preprint arXiv:2010.02502*, 2020. 5, 14
- [65] Anastasis Sathopoulos, Ligong Han, and Dimitris Metaxas. Score-guided diffusion for 3d human recovery. In *Proceedings of the IEEE/CVF conference on computer vision and pattern recognition*, pages 906–915, 2024. 3
- [66] Jianlin Su, Murtadha Ahmed, Yu Lu, Shengfeng Pan, Wen Bo, and Yunfeng Liu. Roformer: Enhanced transformer with rotary position embedding. *Neurocomputing*, 568:127063, 2024. 3
- [67] Yu Sun, Wu Liu, Qian Bao, Yili Fu, Tao Mei, and Michael J Black. Putting people in their place: Monocular regression of 3D people in depth. In *Proceedings of the IEEE/CVF Conference on Computer Vision and Pattern Recognition*, pages 13243–13252, 2022. 2
- [68] Yu Sun, Qian Bao, Wu Liu, Tao Mei, and Michael J Black. TRACE: 5D temporal regression of avatars with dynamic cameras in 3D environments. In *Proceedings of the IEEE/CVF Conference on Computer Vision and Pattern Recognition*, pages 8856–8866, 2023. 2, 7
- [69] Zachary Teed and Jia Deng. DRPOID-SLAM: Deep visual slam for monocular, stereo, and RGB-D cameras. *Advances in Neural Information Processing Systems*, 34:16558–16569, 2021. 2
- [70] Zachary Teed, Lahav Lipson, and Jia Deng. Deep patch visual odometry. *Advances in Neural Information Processing Systems*, 36, 2024. 2
- [71] Guy Tevet, Sigal Raab, Brian Gordon, Yoni Shafir, Daniel Cohen-or, and Amit Haim Bermano. Human motion diffu-

- sion model. In *International Conference on Learning Representations*, 2023. 2, 3
- [72] Garvita Tiwari, Dimitrije Antić, Jan Eric Lenssen, Nikolaos Sarafianos, Tony Tung, and Gerard Pons-Moll. Pose-NDF: Modeling human pose manifolds with neural distance fields. In *European Conference on Computer Vision*, pages 572–589, 2022. 3
- [73] Aaron Van Den Oord, Oriol Vinyals, et al. Neural discrete representation learning. *Advances in neural information processing systems*, 30, 2017. 2
- [74] Ashish Vaswani, Noam Shazeer, Niki Parmar, Jakob Uszkoreit, Llion Jones, Aidan N Gomez, Lukasz Kaiser, and Illia Polosukhin. Attention is all you need. *Advances in Neural Information Processing Systems*, 30, 2017. 2
- [75] Timo Von Marcard, Roberto Henschel, Michael J Black, Bodo Rosenhahn, and Gerard Pons-Moll. Recovering accurate 3d human pose in the wild using imus and a moving camera. In *European Conference on Computer Vision*, pages 601–617, 2018. 2, 6, 13, 14
- [76] Yufu Wang, Ziyun Wang, Lingjie Liu, and Kostas Daniilidis. TRAM: Global trajectory and motion of 3d humans from in-the-wild videos. In *European Conference on Computer Vision*, 2024. 2, 6, 7
- [77] Yufu Wang, Yu Sun, Priyanka Patel, Kostas Daniilidis, Michael J Black, and Muhammed Kocabas. Promptmr: Promptable human mesh recovery. In *Proceedings of the Computer Vision and Pattern Recognition Conference*, pages 1148–1159, 2025. 2, 5, 6, 8
- [78] Donglai Xiang, Hanbyul Joo, and Yaser Sheikh. Monocular total capture: Posing face, body, and hands in the wild. In *Proceedings of the IEEE/CVF Conference on Computer Vision and Pattern Recognition*, pages 10965–10974, 2019. 2
- [79] Hongyi Xu, Eduard Gabriel Bazavan, Andrei Zanfir, William T Freeman, Rahul Sukthankar, and Cristian Sminchisescu. GHUM & GHUML: Generative 3D human shape and articulated pose models. In *Proceedings of the IEEE/CVF Conference on Computer Vision and Pattern Recognition*, pages 6184–6193, 2020. 2
- [80] Yufei Xu, Jing Zhang, Qiming Zhang, and Dacheng Tao. VITPose: Simple vision transformer baselines for human pose estimation. *Advances in Neural Information Processing Systems*, 35:38571–38584, 2022. 13
- [81] Xitong Yang, Devansh Kukreja, Don Pinkus, Anushka Sagar, Taosha Fan, Jinhyung Park, Soyong Shin, Jinkun Cao, Jiawei Liu, Nicolas Ugrinovic, et al. Sam 3d body: Robust full-body human mesh recovery. *arXiv preprint arXiv:2602.15989*, 2026. 5, 13
- [82] Vickie Ye, Georgios Pavlakos, Jitendra Malik, and Angjoo Kanazawa. Decoupling human and camera motion from videos in the wild. In *Proceedings of the IEEE/CVF Conference on Computer Vision and Pattern Recognition*, pages 21222–21232, 2023. 2, 3, 7, 14
- [83] Ye Yuan, Umar Iqbal, Pavlo Molchanov, Kris Kitani, and Jan Kautz. GLAMR: Global occlusion-aware human mesh recovery with dynamic cameras. In *Proceedings of the IEEE/CVF Conference on Computer Vision and Pattern Recognition*, pages 11038–11049, 2022. 2, 7
- [84] Ye Yuan, Jiaming Song, Umar Iqbal, Arash Vahdat, and Jan Kautz. Physdiff: Physics-guided human motion diffusion model. In *Proceedings of the IEEE/CVF international conference on computer vision*, pages 16010–16021, 2023. 5, 15
- [85] Andrei Zanfir, Eduard Gabriel Bazavan, Mihai Zanfir, William T Freeman, Rahul Sukthankar, and Cristian Sminchisescu. Neural descent for visual 3D human pose and shape. In *Proceedings of the IEEE/CVF Conference on Computer Vision and Pattern Recognition*, pages 14484–14493, 2021. 13
- [86] Hongwen Zhang, Yating Tian, Xinchu Zhou, Wanli Ouyang, Yebin Liu, Limin Wang, and Zhenan Sun. PyMAF: 3D human pose and shape regression with pyramidal mesh alignment feedback loop. In *Proceedings of the IEEE/CVF International Conference on Computer Vision*, pages 11446–11456, 2021. 2, 5
- [87] Mingyuan Zhang, Zhongang Cai, Liang Pan, Fangzhou Hong, Xinying Guo, Lei Yang, and Ziwei Liu. Motioidiffuse: Text-driven human motion generation with diffusion model. *IEEE transactions on pattern analysis and machine intelligence*, 46(6):4115–4128, 2024. 3
- [88] Siwei Zhang, Qianli Ma, Yan Zhang, Zhiyin Qian, Taeyun Kwon, Marc Pollefeys, Federica Bogo, and Siyu Tang. EgoBody: Human body shape and motion of interacting people from head-mounted devices. In *European Conference on Computer Vision*, pages 180–200. Springer, 2022. 6, 8
- [89] Siwei Zhang, Qianli Ma, Yan Zhang, Zhiyin Qian, Taeyun Kwon, Marc Pollefeys, Federica Bogo, and Siyu Tang. EgoBody: Human body shape and motion of interacting people from head-mounted devices. In *European conference on computer vision*, pages 180–200. Springer, 2022. 2
- [90] Siwei Zhang, Bharat Lal Bhatnagar, Yuanlu Xu, Alexander Winkler, Petr Kadlecik, Siyu Tang, and Federica Bogo. Rohm: Robust human motion reconstruction via diffusion. In *Proceedings of the IEEE/CVF Conference on Computer Vision and Pattern Recognition*, pages 14606–14617, 2024. 2, 3

# DuoMo: Dual Motion Diffusion for World-Space Human Reconstruction

## Supplementary Material

### A. Sparse mesh representation

#### A.1. Topology

We use a sparse mesh  $\mathbf{X} \in \mathbb{R}^{V \times 3}$  to represent the human body and its motion. The sparse mesh has  $V = 595$  vertices [16], and is designed to balance between representation quality and efficiency. Figure 7a shows the sparse mesh topology. Specifically, the vertices are positioned to ensure that body pose, shape, and hand gestures are accurately represented despite the sparsity. Consistent with prior methods [46, 54], skeletal joints are regressed from the posed mesh using linear combinations of local vertices.

#### A.2. SMPLX to sparse mesh

To leverage existing datasets for training our motion models, we create regression matrices to convert SMPL or SMPLX meshes to the sparse mesh, using a strategy similar to learning the joint regressor for SMPL [46]. Each vertex on the sparse mesh can be computed as a weighted average of a sparse set of vertices from the SMPL/SMPLX models.

With the regressor matrices, we convert training datasets [5, 49, 75] to the sparse mesh format. Figure 7b visualizes an example from the BEDLAM dataset [5] with its annotation converted to our sparse mesh format.

#### A.3. Sparse mesh to SMPLX

Our sparse mesh can represent detailed motion, but converting it to SMPLX provides a more compact representation and is necessary to compare reconstruction accuracy with prior works.

The conversion to SMPLX parameters can be achieved through optimization [54, 60], but it is slow and prone to local minima. In contrast, we train an optimization-inspired iterative network [11, 63, 85] for this task.

Our network performs iterative refinement using a cascade of three MLPs, as shown in Figure 8. The process begins with zero-initialized SMPLX parameters. At each stage, we generate a predicted sparse mesh from the current SMPLX parameters, using the SMPLX layer followed by our sparse regressor A.2. We then rigidly align the prediction to the target sparse mesh using the head vertices, and compute the per-vertex errors. The MLP takes the errors as input and predicts an update to the parameters. We repeat this process for two more stages. This cascaded design allows each MLP to specialize its refinement.

We tested the network on 3DPW [75] and find the MPJPE error to be under 5mm. We visualize some qualitative results in Figure 9.

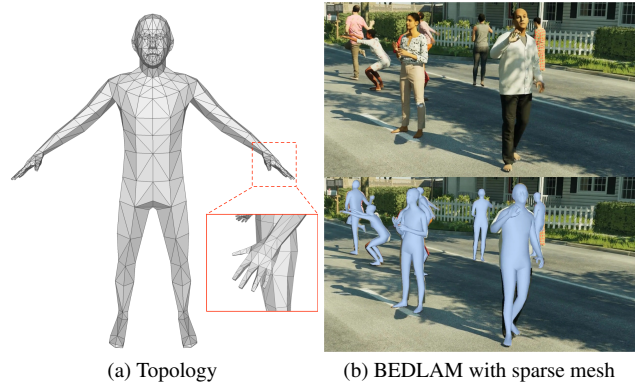


Figure 7. **Sparse mesh.** (a) Topology of our sparse mesh, with the red box showing the details of the hands. (b) An example from the BEDLAM [5] dataset with its annotation converted to the sparse mesh format.

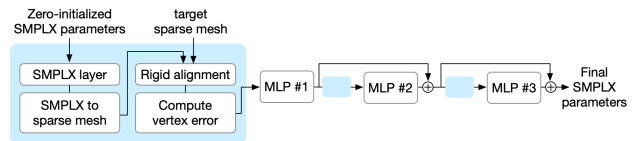


Figure 8. **Architecture (sparse mesh to SMPLX).** This network performs iterative refinement to predict SMPLX parameters from a target sparse mesh.

### B. Dense keypoint detection

The dense 2D keypoints are defined to semantically correspond to the 3D vertices of our sparse mesh. We used the conditional dense body keypoint detection model from SAM 3D Body [81] to infer these 595 body surface keypoints. This model takes a human-centered image and a set of 23 sparse human body keypoints as condition to estimate the dense surface points. We leverage the synthetic dataset BEDLAM [5] to train the network, where the backbone weights were initialized with ViTPose [80] to maintain the generalizability to the real images. During inference, we first run ViTPose to extract the sparse 23 keypoints from the input images, which are then fed into the network as the conditioning signal to predict the final 595 dense body surface keypoints. When training the diffusion models, the dense keypoint detection model is frozen.

Figure 10 visualizes keypoint detection results on the EMDB dataset [28]. Edges from the sparse mesh are added to improve visualization clarity.

## C. Experiment details

### C.1. Training

We train our camera-space model and world-space model with similar setups. We train each model with 8 H200 GPUs, with a batch size of 32 per GPU leading to an effective batch size of 256. The sequence length  $T$  is 120 frames.

**Architecture.** We use the same diffusion transformer (DiT) [55] architecture for the two motion models. It has 8 self-attention layers with  $d_{\text{model}} = 512$ , each with 8 heads for multi-head attention, and a hidden dimension of 2048 for the feedforward layer.

**Data.** To train our camera-space motion model, we use AMASS [49], Goliath [50], BEDLAM [5] and 3DPW [75]. For AMASS and Goliath, we generate the 2D dense keypoints from the ground truth annotation and do not use images. For BEDLAM and 3DPW, we generate the 2D dense keypoints and use PromptHMR to extract image features.

To train our world-space motion model, we use AMASS [49], BEDLAM [5] and 3DPW [75]. We use the same procedure as training the camera-space model to generate the inputs. We then use the frozen camera-space model and lifting to generate the inputs for the world-space model training.

We train the dense keypoint detection model with BEDLAM by generating 2D dense keypoints from the ground truth annotation. We train the Sparse-mesh-to-SMPLX iterative network with BEDLAM and 3DPW.

**Augmentation.** We employ data augmentation and an augmentation in diffusion noise sampling during training.

We apply augmentation to the generated 2D dense keypoints for training the motion models. We apply noise, perturbation, and masking to the keypoints to simulate detection errors. We apply these augmentation at the point level (e.g. by sampling a set of keypoints) and at the part level (e.g. by applying the same perturbation or masking to all keypoints in a body part).

For training the diffusion models, we apply an augmentation to the sampling of diffusion time step  $k$ . For 50% of the samples, we uniformly sample time steps from  $\{1, \dots, 1000\}$  similar to the standard diffusion training [23, 64]. For 50% of the samples, we set  $k = 1000$ , corresponding to the highest level of corruption. This is equivalent to the “estimation mode” in GENMO [38], which finds this strategy encourages the diffusion model to produce good estimation during early diffusion steps.

### C.2. Evaluation metrics

**Camera-space reconstruction.** We evaluate our model’s camera-space reconstruction accuracy using three metrics:



Figure 9. **Sparse mesh to SMPLX estimation.** Examples of the predicted SMPLX mesh (black) overlaid on the target sparse mesh (white).

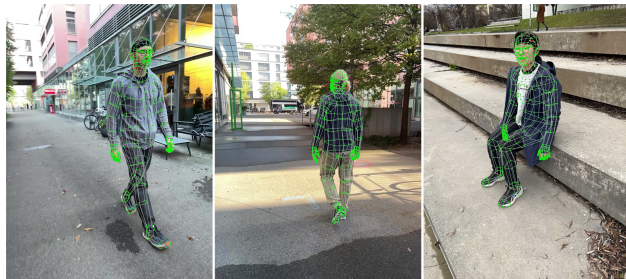


Figure 10. **Dense keypoint detection** on the EMDB dataset [28]. Edges added for visualization only.

MPJPE, PA-MPJPE, and PVE. The MPJPE (mean per-joint position error) aligns the prediction with the ground truth at the pelvis location (removing translation) and measures the mean squared error (MSE) on the 3D joints. The PA-MPJPE (Procrustes-aligned MPJPE) rigidly aligns the prediction and ground truth 3D joints (removing rotation, translation and scale) before calculating the MSE on 3D joints. Finally, the PVE (per-vertex error) aligns the predicted and ground truth meshes at the pelvis (removing translation) and computes MSE on the vertices.

**World-space reconstruction.** We evaluate world-space reconstruction accuracy with WA-MPJPE, W-MPJPE, RTE, Jitter and Foot sliding. WA-MPJPE and W-MPJPE both measure 3D joints MSE on 100-frame segments of prediction with the ground truth, but differ in how they align the prediction with the ground truth. WA-MPJPE aligns the whole segment (e.g. 3D joints across 100 frames) while W-MPJPE aligns the first two frame (e.g. 3D joints in the first two frames) [82]. Intuitively, WA-MPJPE measures the accuracy and coherence of the 100-frame motion snippet, while W-MPJPE additionally measures drift.

RTE (root trajectory error) measures the accuracy of the whole trajectory. It rigidly aligns the trajectories of the root and computes the mean square error in the unit of %. Jitter uses finite difference to compute the jerk on the 3D joints to access motion smoothness. Finally, foot sliding calculates the displacement on the predicted foot vertices on contact frames to measure erroneous sliding.

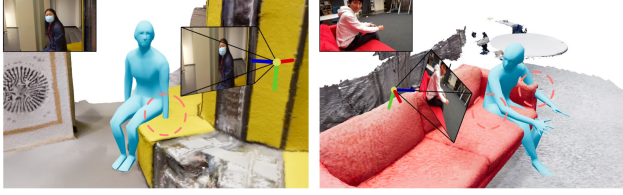


Figure 11. **Limitation 1.** Because our models do not incorporate 3D scene information, the results exhibit inconsistencies in fine-grained details.



Figure 12. **Limitation 2.** In challenging poses, the generated sparse meshes sometime exhibit unrealistic deformation. Converting them to SMPL meshes (sec A.3) partially improves the results.

### C.3. Limitations

While DuoMo achieves a new state-of-the-art in world-space human motion reconstruction, it has several limitations that we want to address in future works.

**Scene awareness.** While we demonstrated that DuoMo can generate scene-consistent motion with guided sampling in the Experiment section, the 3D scene information is not explicitly used. Figure 11 illustrates some failures in terms of human-scene inconsistency. Future works could incorporate scene information or other physics-based objectives in the guided sampling process [84] to improve such scenarios. Another direction is to train a world-space motion model that can take 3D scene information as auxiliary conditioning.

**Uncertainty awareness.** We have modeled visibility at the keypoint level and the frame level, by replacing the embeddings of occluded keypoints or frames with null tokens (Method section). However, the keypoint visibility is determined by thresholding detection confidence, a procedure that is not always accurate. Turning detection confidence into a binary visibility label also discards information. Future work could improve accuracy of the motion model by integrating uncertainty reasoning with detection confidence.

**Mesh generation robustness.** We demonstrate that our architecture can generate the motion of mesh vertices, but in difficult cases the generated meshes could have unrealistic deformation. Figure 12 shows examples of deformed meshes. One interesting direction is to integrate our architecture with a tokenized or latent representation of the sparse mesh [17, 42] in the form of latent diffusion [58].